



Microstructural evolution and pitting corrosion behavior of friction stir welded joint of high nitrogen stainless steel



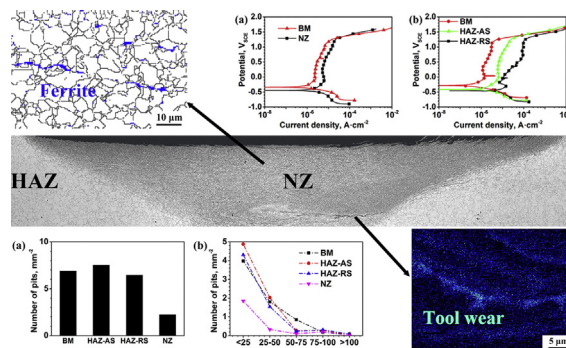
H. Zhang, D. Wang, P. Xue, L.H. Wu, D.R. Ni, Z.Y. Ma *

Shenyang National Laboratory for Materials Science, Institute of Metal Research, Chinese Academy of Sciences, 72 Wenhua Road, Shenyang 110016, China

HIGHLIGHTS

- Pitting corrosion behavior of high nitrogen steel joint was studied after friction stir welding.
- No drastic decrease in breakdown potentials was observed in the heat affected zones.
- Nugget zone showed good pitting corrosion resistance due to microstructural changes.
- δ -ferrite and tool wear bands were detected in friction-stir weld zone of high nitrogen stainless steel.
- Pitting corrosion resistance of the nugget zone was found to be unaffected by δ -ferrite and tool wear.

GRAPHICAL ABSTRACT



ARTICLE INFO

Article history:

Received 9 May 2016

Received in revised form 3 August 2016

Accepted 14 August 2016

Available online 15 August 2016

Keywords:

High nitrogen stainless steel

Friction stir welding

Pitting corrosion

Microstructure

ABSTRACT

With the achievement of sound joints of high nitrogen stainless steel via friction stir welding, significant microstructural changes take place in various regions of the joints. This would bring out the change in the corrosion properties of the joints. In this study, the corrosion behavior of friction stir welded joint of high nitrogen stainless steel was investigated using electrochemical and immersion tests. No drastic decrease in breakdown potentials was observed in the heat affected zones with number and size distribution densities of pits being similar to that in the base metal. The nugget zone exhibited a relatively good pitting corrosion resistance, mainly attributing to the breakup of coarse inclusions and grain refinement during welding. The δ -ferrite bands and tool wear exerted no obvious effects on the corrosion behavior of the welded joint due to the lack of Cr diffusion.

© 2016 Elsevier Ltd. All rights reserved.

1. Introduction

High nitrogen stainless steel (HNS), as a relatively new kind of engineering material, has gained more and more attention, due to the favorable mechanical and corrosion properties. Various kinds of HNS have been utilized in many fields, such as power-generating industry, ship

building, railways, chemical equipment, petroleum and nuclear industries. Nitrogen as a powerful austenite-stabilizing element can not only improve the strength and fracture toughness of HNS significantly, but also increase the pitting corrosion resistance of steels [15,24].

The wide application of HNS in industrial fields requires effective and reliable joining methods. However, the high nitrogen content brings some difficulties in the welding of HNS. The fusion welded joints of HNS have defects such as blowhole, weld cracking and nitrogen loss, especially for HNS with higher nitrogen content. In this case, the corrosion resistance of fusion welded joints of HNS was significantly

* Corresponding author.

E-mail address: zym@imr.ac.cn (Z.Y. Ma).

decreased [30]. The challenges in the welding seriously hindered the wide use of HNS.

Friction stir welding (FSW) is a solid-state welding method [17], developed in UK. During the FSW process, a rotating tool which consisting of a shoulder and a pin is inserted into the plates and then moved along the joint line, the softened material around the tool by friction heat and plastic deformation is transported from the front of tool to the rear, resulting in the formation of weld under forging force. In this process, no melting of material occurs. Originally, FSW was mainly used for joining low melting-point metals such as aluminum and magnesium [8,28,32]. Later, with the development of welding tools, FSW has been successfully applied in the welding of high melting-point materials, such as different kinds of steels [22,33], titanium and its alloys [31,34].

FSW may become one of the promising joining methods of HNS due to its distinct advantages. The possibility of applying FSW for the joining of HNS (23.1Cr-10.1Ni-5.9Mn-2.0Mo-0.2Si-0.02C-0.53N) was for the first time tried by Park et al. [20]. The results showed that no loss of nitrogen was detected in the nugget zone (NZ) and the coarse grains were refined during the FSW process. However, some defects were observed in the welded joint. In order to determine the optimum welding condition, Miyano et al. [18] tried different welding parameters and finally obtained defect-free joints of HNS. The joints showed higher hardness and strength compared to the base material (BM). For the purpose of further investigating the microstructure evolution and the strength of FSW HNS joint, TEM observation and full gage length tension were conducted by Wang et al. [29]. It was indicated that no sigma phase was observed in the NZ and the strength of the joint was similar to that of the BM.

As a relatively new kind of stainless steel, the corrosion properties of HNS are very important to the practical applications, and can be influenced by many factors. It was reported that due to the high nitrogen content of HNS, the precipitation of Cr_2N occurred during aging, and seriously deteriorated the pitting corrosion resistance [10]. Furthermore, during the welding process, δ -ferrite could form in the welded joints. Moon et al. [19] found that both pitting corrosion resistance and inter-phase corrosion resistance were deteriorated by δ -ferrite formation due to the formation of Cr-depleted zones along ferrite.

Grain size can also produce an effect on the corrosion resistance of HNS. Schino and Kenny [6] came to a conclusion that with smaller grain size the inter-granular corrosion resistance and pitting corrosion resistance of HNS were improved, however, the general corrosion resistance was decreased. Furthermore, high defect density and deformation bands introduced by cold work could also lead to a less protective passive film on HNS in a 3.5% NaCl solution [7,11]. During the FSW process, severe plastic deformation and thermal cycle would lead to an obvious change in the microstructure of HNS, and then further influence the corrosion properties.

Although the HNS joints with good mechanical properties can be achieved via FSW, the studies on the corrosion properties of the FSW HNS joints are relatively limited. Li et al. [14] studied the microstructure and corrosion properties of FSW HNS, and the results showed that a

small amount of Cr_{23}C_6 was detected in the NZ and the corrosion resistance of the NZ was slightly decreased. Compared to fusion welded joints, the FSW HNS joints with low heat-input have a far different microstructure and therefore it is of practical importance to understand the effect of the microstructural evolution on the corrosion behavior of FSW HNS joints.

In this study, the microstructure and pitting corrosion resistance of FSW HNS joints are investigated. The purpose is to understand the key factors influencing the pitting corrosion resistance of FSW HNS joints to provide guidance to the optimization of FSW parameters. For easy understanding, the acronyms in the field of FSW are given in Table 1.

2. Experimental

1.8 mm thick hot-rolled HNS plates were used in this study, and the chemical compositions of HNS are listed in Table 2. Before FSW the plates were subjected to solid solution treatment at 1100 °C for 2 h. FSW was performed at a welding speed of 50 mm/min and a tool rotating speed of 500 rpm, using a W-Re alloy tool with an 11-mm-dia shoulder and 5.7-mm-dia cylindrical pin with a length of 1.6 mm. An argon gas shield was employed during the welding process to prevent the oxidation of the joint.

The cross-section of the joint perpendicular to the welding direction was subjected to microstructural observations by optical microscopy (OM) and scanning electron microscopy (SEM). The polished specimen was electrolytically etched in a 10% oxalic acid solution. X-ray diffraction (XRD) and electron backscattered diffraction (EBSD) were used to analyze the phases. Specimens for EBSD analysis was prepared by electrolytic polishing with a 10% perchloric acid, 90% ethanol solution at 30 V. Electron probe micro-analyzer (EPMA) was used to identify the element distribution. Temperature history of heat-affected zone (HAZ) was recorded by a K type thermocouple at the location of 6 mm from the weld center.

Ferric chloride pitting test was used to evaluate the corrosion resistance of the welded joint. Following Method A in ASTM G48 standard [2] for immersion test, specimens were immersed in 6% FeCl_3 solution (by mass) for 72 h, and the temperature during the test was 50 ± 2 °C. The quantity and size distribution densities of pits were statistically analyzed based on OM observations. Electrochemical tests were carried out using a three-electrode electrochemical cell, i.e. saturated calomel reference electrode (SCE), a planar Pt counter electrode and the specimen as a working electrode. The specimens were brazed to a copper wire and then cold mounted in epoxy resin. Fig. 1 shows the sampling location in both NZ and HAZ.

The exposed surface areas of the NZ and HAZ specimens were 0.22 cm² and 0.62 cm², respectively. The specimens were mechanically ground up to 1000 grit with SiC abrasive papers. Gamry reference 600 potentiostat was used for corrosion tests. In order to determine corrosion properties, potentiodynamic polarization test, potentiostatic polarization test and electrochemical impedance spectroscopy (EIS) were used. All of the electrochemical tests were performed after immersion in 3.5 wt.% NaCl solution for 30 min. The applied potential of potentiodynamic polarization test ranged from $-0.5 V_{\text{SCE}}$ to $+2 V_{\text{SCE}}$ with a scan rate of 0.5 mV/s, and potentiostatic polarization test was conducted

Table 1
Acronyms of friction stir welding.

Acronyms	Full words
HNS	High nitrogen stainless steel
FSW	Friction stir welding
BM	Base material
NZ	Nugget zone
HAZ	Heat affected zone
TMAZ	Thermo-mechanically affected zone
AS	Advancing side
RS	Retreating side

Table 2
Chemical compositions of BM (wt.%).

C	Mn	Cr	Mo	N	Fe
0.04	15.81	18.36	2.19	0.66	Bal.

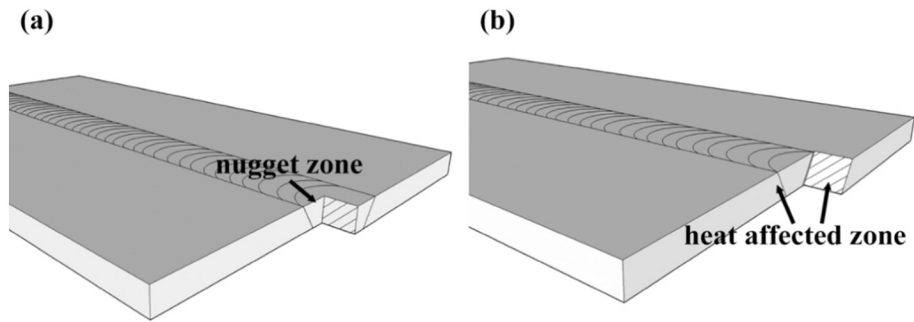


Fig. 1. Scheme of extraction of electrochemical testing samples: (a) sampling location of NZ, (b) sampling location of HAZ.

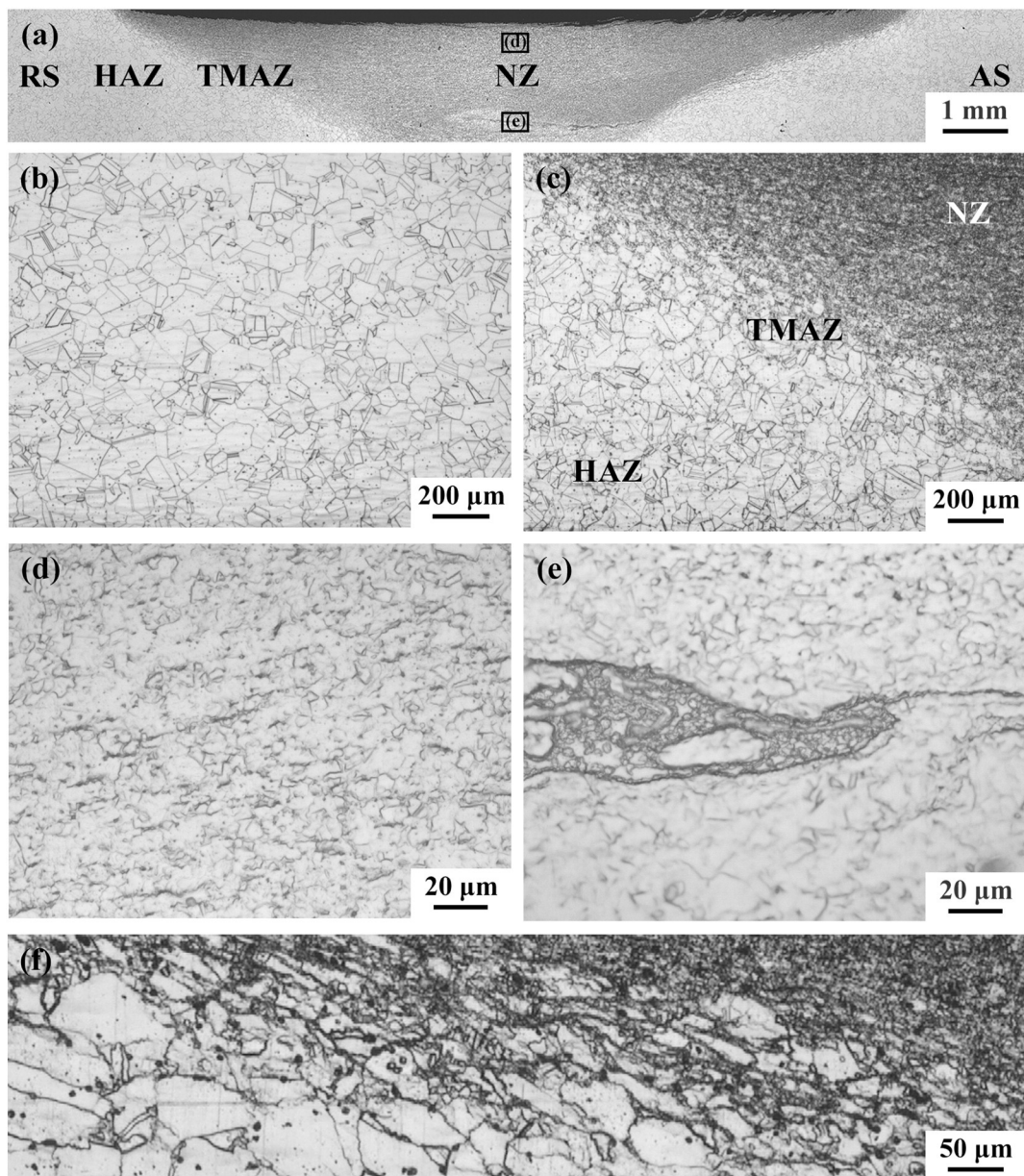


Fig. 2. Optical macrograph showing the microstructure of transverse section of FSW joint: (a) optical macrograph of the joint (advancing side (AS) of the joint is on the right while retreating side (RS) is on the left), (b) BM, (c) TMAZ and HAZ, (d) top of NZ, (e) bottom of NZ, (f) magnified view of TMAZ showing deformed microstructure.

at 0.4 V_{SCE} , and the potential was in the range of the passive region according to the potentiodynamic polarization curves. EIS measurements were carried out from 100 kHz to 10 mHz with a 5 mV perturbation at the open circuit potential (OCP). The electrochemical tests were repeated at least three times.

3. Results

Fig. 2(a) shows the cross-sectional optical macrograph of a FSW HNS joint after electrolytically etching. Defect-free joint was achieved by FSW at a welding speed of 50 mm/min and a tool rotating speed of 500 rpm. The joint could be divided into three typical zones: NZ, thermo-mechanically affected zone (TMAZ) and HAZ. As shown in Fig. 2(b), the BM had a typical annealed coarse grain structure in which many annealing twin boundaries were observed, the average grain size of the BM was about 50 μm . Fig. 2(c) shows the microstructure of the HAZ and TMAZ. The HAZ exhibited roughly the same coarse grain microstructure with twin boundaries as the BM. The TMAZ, on the other hand, exhibited a deformed microstructure with elongated grains being unevenly distributed, which was the result of experiencing thermal cycle and deformation during welding. A magnified microstructure of the TMAZ is given in Fig. 2(f).

As shown in Fig. 2(d), the NZ, affected by the rotating tool pin, had a fine microstructure with roughly equiaxed grains, suggesting that the NZ underwent dynamic recrystallization due to the frictional heating and severe plastic deformation during the FSW process. The grain size of the NZ was roughly 5 μm and much finer than that of the BM. It should be noted that some small bands were observed in the top of the NZ (outlined in black frame in Fig. 2(a)), the distribution of these discontinuous bands was relatively dispersive. In the bottom layer of the NZ, a coarse continuous band was observed. As shown in Figs. 2(a) and (e), this dark-etched band structure extended to the advancing side (AS) of the NZ with a wavy shape.

Fig. 3 shows the XRD profiles of the NZ and BM. It was indicated that the BM was fully austenite after solid solution treatment whereas the NZ had a mixed microstructure of austenite and ferrite, though the fraction of ferrite phase was relatively low. EBSD map of the NZ is shown in Fig. 4. The austenitic grains in the NZ were roughly equiaxed, and low angle grain boundaries were observed in the austenitic grains. The discontinuous bands in the NZ observed in Fig. 2(d) were identified as newly formed δ -ferrite. The formation of δ -ferrite during FSW was observed in previous studies [18,29]. EPMA of the band structure in the bottom of the NZ indicated that the distribution of chromium was roughly uniform, however, the distribution of tungsten was inhomogeneous, and W-rich band-like structure was observed in the bottom of the NZ (Fig. 5).

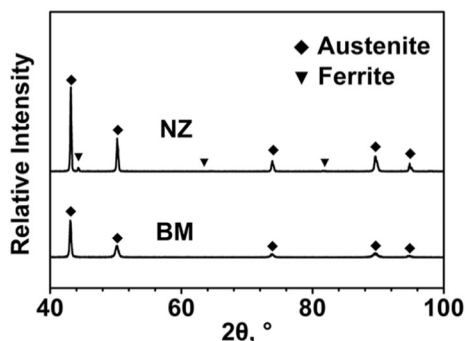


Fig. 3. XRD profiles of NZ and BM.

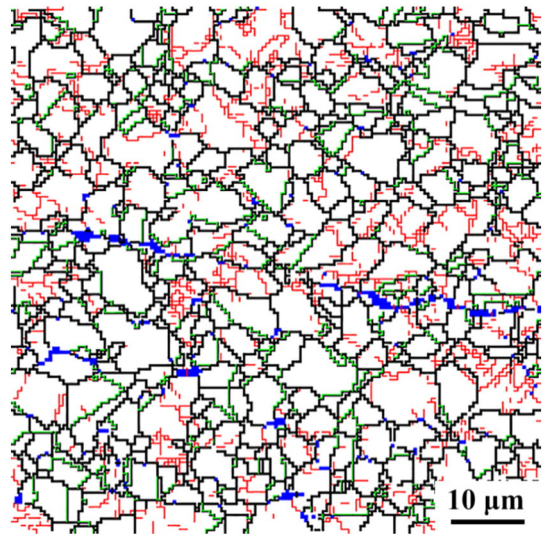


Fig. 4. Phase distribution map of NZ (white and blue grains denote austenite and ferrite, respectively. Black, red and green lines indicate high-angle boundaries, low-angle boundaries, and twin boundaries, respectively).

The surface morphologies of welded joint subjected to ferric chloride pitting immersion test and electrolytically etching in a 10% oxalic acid solution are shown in Figs. 6(a) and (b). The pitting distribution of the BM was relatively scattered, pits were often observed in the neighborhood of inclusions as shown in Fig. 7(a) and at the grain boundaries as shown in Fig. 7(b). Fig. 7(c) shows a typical pit in the HAZ. It is noted that the diameter of the pits in the HAZ was similar to that in the BM (Figs. 7(a) and (b)). A few relatively large pits and some small pits could be observed in both the HAZ and BM. In the NZ, the pits were very small and scattered as shown in Fig. 7(d), no large pits were found. It should be noted that few pits were observed near ferrite phase, implying that the neighborhood of ferrite had no strong tendency of pitting.

Fig. 8 shows the potentiodynamic polarization curves of the NZ, HAZ and BM specimens. The curves exhibited similar trend, a wide range of passivity was observed beyond the open-circuit potential. Electrochemical parameters obtained from potentiodynamic polarization curves are listed in Table 3.

The corrosion potential (E_{corr}) of the NZ was slightly lower than that of the BM, and the corrosion current density (i_{corr}) and passivation current density (i_p) of the NZ were slightly higher. However, it is noted that the breakdown potential (E_b) of the NZ was slightly higher than that of the BM. The E_b of the HAZ was also close to that of the BM while the E_{corr} of the HAZ was lower than that of the BM. And i_{corr} and i_p of the HAZ appeared higher. It is noted that the HAZ specimens on the AS showed higher i_{corr} and i_p , and lower E_{corr} than those on the retreating side (RS). Both the NZ and HAZ specimens showed slightly more tendency to corrosion in electrochemical polarization tests, however, no serious decrease in E_b indicated that no strong tendency of pitting occurred during the tests, which agreed with the results of immersion test.

To study the protectiveness of the passive film, potentiostatic polarization tests were conducted. Current density-time curves are given in Fig. 9. The passive film of the BM showed good protective capability and stability, and no obvious current density fluctuation was observed. The current density in the NZ was very close to that in the BM. The HAZ specimens showed higher current density during polarization

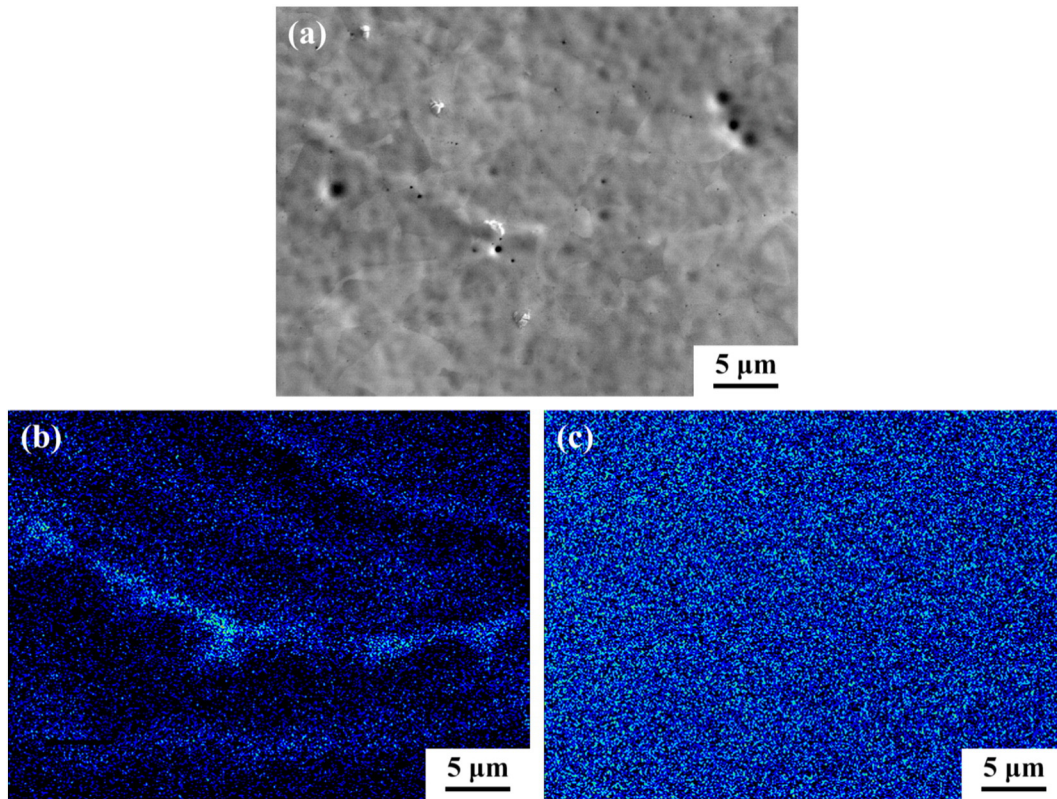


Fig. 5. EPMA map of element distribution of the bottom band of NZ: (a) SEM image of the selected zone, (b) distribution of tungsten, (c) distribution of chromium.

compared with the BM specimens, therefore the oxide film in the HAZ was less protective.

EIS results are shown in Fig. 10, and the Nyquist plots are analyzed using the equivalent electrical circuit and given in Fig. 11. R_{sol} represents the electrolyte resistance and other ohmic resistance, R_2 represents the film resistance, R_1 corresponds to the resistance inside the film pores, Q includes the pseudocapacitance of the film, expressed using the constant phase element (CPE), C stands for the double layer capacity [9].

The variation of film resistance (R_2) is given in Fig. 12. Film resistance of the BM was slightly higher than that of the NZ, and the film resistance of the HAZ appeared lower, i.e., the protective film of the BM and NZ showed relatively good stability. Fig. 13 shows the Bode plots of the different zones of the FSW HNS joint. The BM and NZ showed similar impedance, however, the HAZ specimens showed inferior corrosion resistance. The result of electrochemical tests implies that the passive film of the NZ and HAZ was less protective compared to that of the BM. However, the E_b of the NZ and HAZ specimens were higher than

or very close to that of the BM specimens, indicating that no decrease in pitting corrosion resistance occurred in the NZ and HAZ.

4. Discussion

After static immersion in 6% FeCl_3 solution (by mass) for 72 h, the distribution density and size of the pits of the joint were statistically analyzed, and results are shown in Fig. 14. As can be seen in Figs. 14(a) and (b), the number and size distribution of the pits in the HAZ were very similar to that in the BM. Nevertheless, in the NZ both number and size distribution densities of the pits were distinctly decreased. These results agreed well with the potentiodynamic polarization results. The wide range of passivity indicated that high nitrogen stainless steel showed great corrosion resistance, and slightly higher E_b implied higher pitting corrosion resistance. The potentiodynamic polarization curves in this study are very similar to those in a previous study [14]. However,

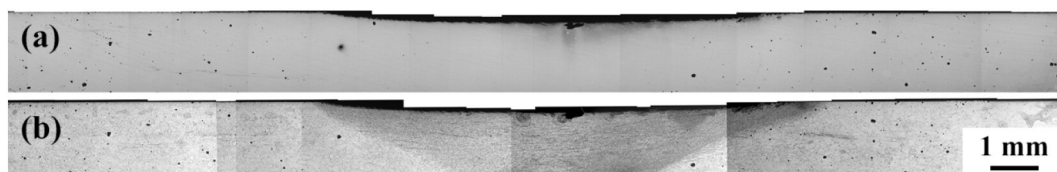


Fig. 6. Pitting morphology of FSW joint after immersion corrosion test for 72 h: (a) without electrolytically etching, (b) with electrolytically etching.

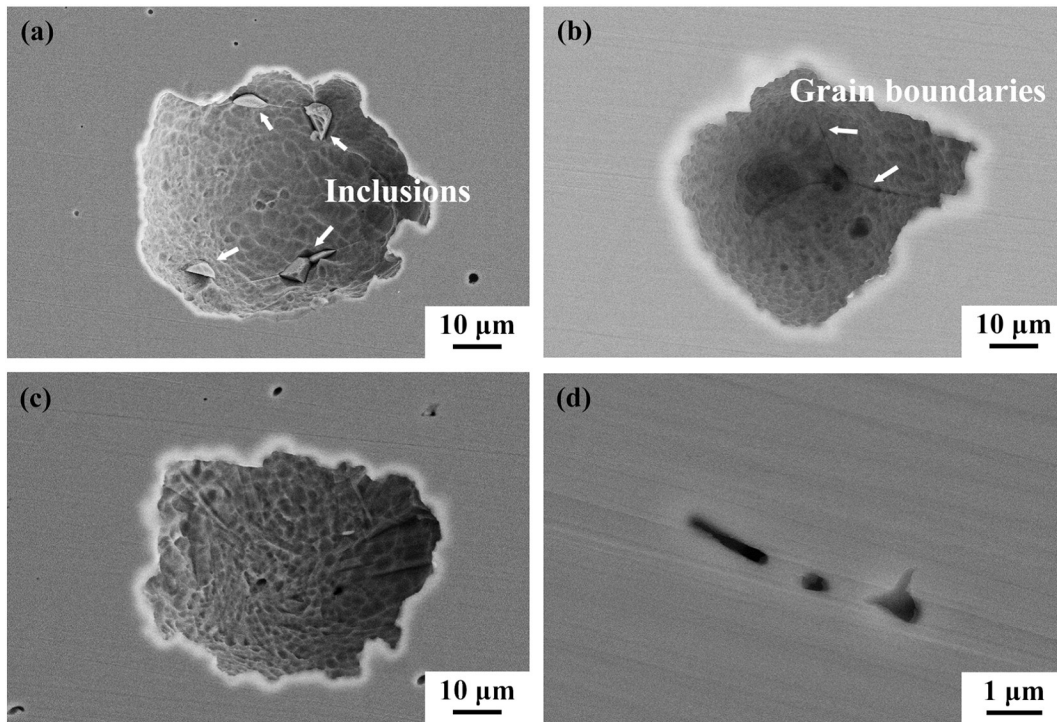


Fig. 7. Pits in different zones of the joint after immersion corrosion test for 72 h: (a), (b) BM, (c) HAZ, (d) NZ.

the decreased E_p was observed in Ref. [14], attributed to the effect of precipitation of $Cr_{23}C_6$.

During the FSW process, significant friction heat and intense plastic deformation were generated by the rotating tool, and dynamic recrystallization occurred in the NZ, therefore the grains in the NZ were significantly refined. However, due to the absence of the precipitation of Cr-rich particles, no obvious decrease of breakdown potential was observed in potentiodynamic polarization test.

Some researchers found that a small number of Cr nitride less than 100 nm in size was formed in the HAZ along the grain boundaries [20]. It has been reported that thermal exposure at temperatures between 700 and 900 °C may result in the precipitation of Cr-rich nitride in stainless steels with relatively high nitrogen content [4,23]. The formation of Cr-rich particles created Cr-depletion zones which are sensitive to corrosion [10]. In our study, the temperature of the HAZ during

FSW was in the temperature range of nitride formation (Fig. 15). The formation of Cr-rich particles is related to the diffusion of Cr atoms, with a relatively long incubation period. Because of relatively low heat-input and high cooling rate of FSW, exposure period at precipitation temperature was short, thus the precipitation of Cr-rich compound should be limited, and this could be the main reason that no serious deterioration in corrosion resistance was detected in the HAZ.

The microstructural evolution during FSW was very complicated. There were many factors that could affect the corrosion resistance, such as the impurity segregation [3,25,35], grain refinement, residual stress [26], precipitated phases [1,5], nitrogen loss, the proportion of coincidence site lattice (CSL) boundaries and low angle boundaries (LABs) [12,13,16].

The pits in the NZ were relatively small, and the distribution of the pits was roughly scattered. FSW is different from traditional fusion

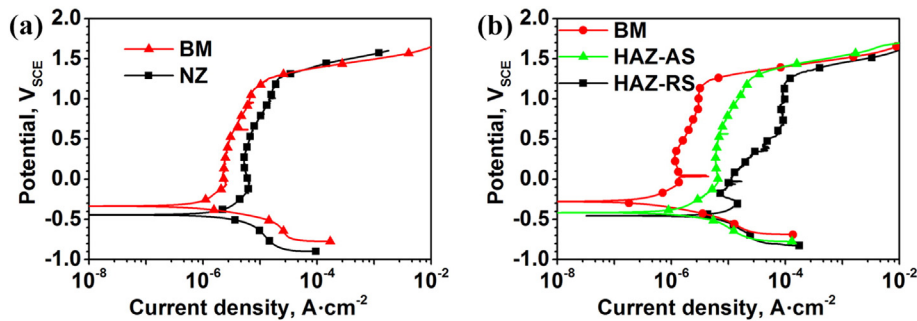


Fig. 8. Potentiodynamic polarization curves of different sampling location specimens: (a) BM and NZ, (b) BM, advancing side HAZ and retreating side HAZ.

Table 3

Electrochemical parameters of various regions of FSW HNS joint obtained from potentiodynamic polarization test in 3.5% NaCl solution.

Sample	$E_{\text{corr}}/V_{\text{SCE}}$	$I_{\text{corr}}/A \cdot \text{cm}^{-2}$ ($\times 10^{-7}$)	E_b/V_{SCE}	$I_p/A \cdot \text{cm}^{-2}$ ($\times 10^{-6}$)	Anodic Tafel slopes
					Cathodic Tafel slopes
BM	-0.31	5.97	1.14	2.73	0.39 -0.15
NZ	-0.45	20.5	1.26	7.14	0.61 -0.22
HAZ-AS	-0.46	66.1	1.20	56.0	0.59 -0.44
HAZ-RS	-0.42	11.4	1.21	9.66	0.42 -0.14

corrosion process, the grain boundaries were corroded as an anode. So the decrease in the grain size led to the increases of anodic area, thus the homogeneity of the specimen increased, which may have positive effects on improving local corrosion resistance. On the other hand, some researchers [21,27] found that the improved corrosion resistance in the fine-grained samples could be attributed to the improvement of passive film stability, and this stable protective film could be the result of increased Cr diffusion rate in fine-grained structures. The grain boundaries were the diffusion paths of alloying elements, Cr atoms were easy to diffuse in the grain boundaries, and thus the capability of protection and repassivation could be improved in fine-grained samples as illustrated in Fig. 16. These may be the reason for that no large pits were observed in the NZ.

During FSW the NZ underwent severe plastic deformation and thermal cycle. δ -ferrite could form when the temperature of the NZ

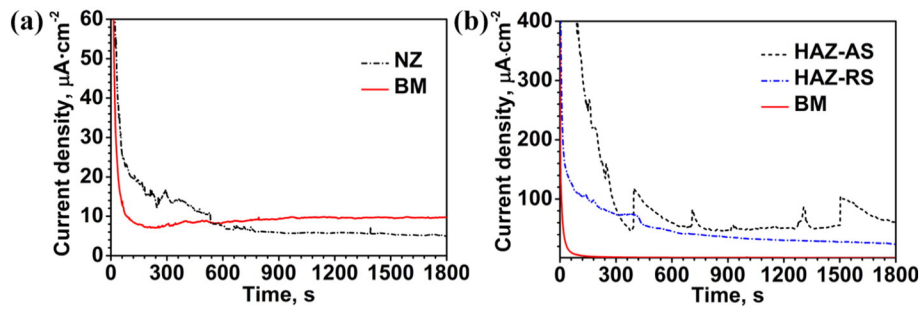


Fig. 9. Potentiostatic polarization current density-time curves of HNS joint, the applied potential was $0.4 V_{\text{SCE}}$: (a) NZ and BM, (b) HAZ and BM.

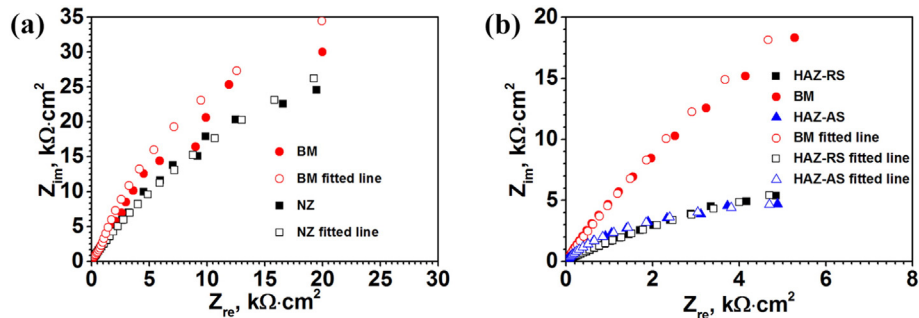


Fig. 10. Nyquist plots of HNS joint, the frequencies were from 100 kHz to 10 mHz with a 5 mV perturbation: (a) NZ and BM, (b) HAZ and BM.

welding in that FSW creates severe deformation and no melting of metals occurs. For this reason, the existent inclusions in the BM were re-dissolved and refined because of thermal cycle and strong stirring effect during welding, which had beneficial effect on the improvement of corrosion resistance. Therefore, no pits caused by large inclusions like those in Fig. 7(a) were observed.

The main difference between the BM and NZ was the grain size. It was reported that grain-refining may have a contribution to the improvement of corrosion resistance [6,27]. During the immersion

exceeded the phase transformation temperature. Due to the friction effect of the tool shoulder, the temperature in the top layer of the NZ was higher than that in the bottom layer, thus the ferrite bands were mainly formed in the top layer. During electrolytically etching in 10% oxalic acid

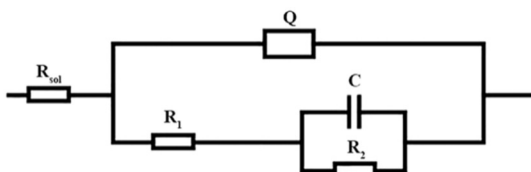


Fig. 11. The equivalent circuit for quantitative evaluation of EIS spectra.

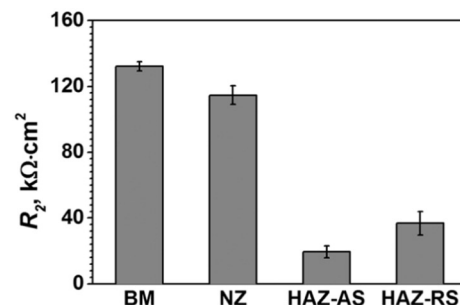


Fig. 12. The variation of film resistance (R_2) of the joint obtained from Nyquist plots.

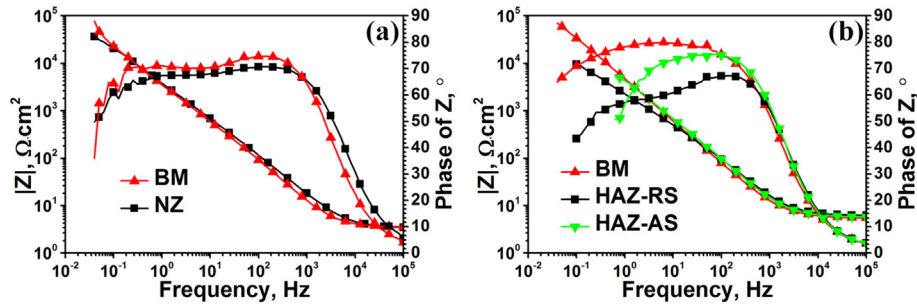


Fig. 13. Bode plots of HNS joint: (a) BM and NZ, (b) BM and HAZ.

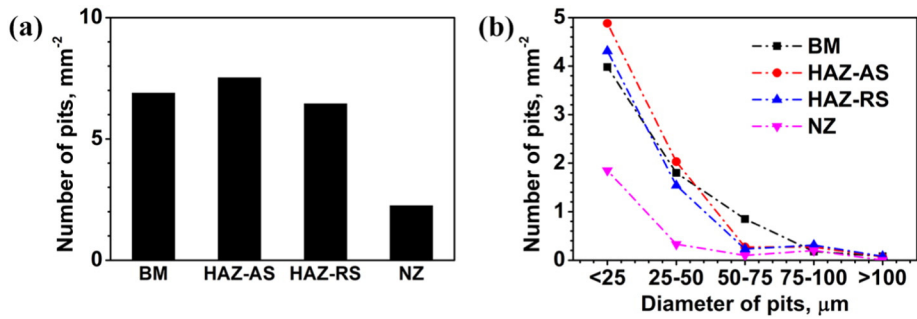


Fig. 14. Statistical analysis of pits after static ferric chloride pitting immersion test for 72 h at 50 °C: (a) number distribution, (b) size distribution.

solution, the ferrite bands were corroded, leaving dark-etched band-structures mainly in the top layer of the NZ.

Fig. 17 shows the EPMA results of Cr element distribution. The locations of ferrite bands with identical morphology in EBSD tests are pointed out by white arrows. The distribution of Cr was roughly uniform and no Cr-depleted zone along ferrite was detected. It was reported that in the HAZs of fusion welding, the formation of δ -ferrite could lead to the decrease in both pitting and intergranular corrosion resistance due to the formation of Cr-depleted zone [19]. However, in this study, no strong tendency for the pitting was detected along ferrite-austenite boundaries, this could also be explained by the low heat-input of FSW. Low heat-input and high cooling rate resulted in the less sufficient diffusion of Cr atoms, therefore the Cr-depleted zone could not form along ferrite and austenite boundaries.

Since the HNS used in this study had no tungsten, it could be deduced that W element in the bottom of the NZ was introduced by wear of W-Re alloy welding tool as confirmed by the EPMA results in Fig. 5. Based on the temperature distribution of the FSW joint, tool wear should mainly occur in the bottom of the pin because of severe friction and relatively low temperature. In the welding process, rotating tool pin carried the wear debris moving around from the RS to the AS.

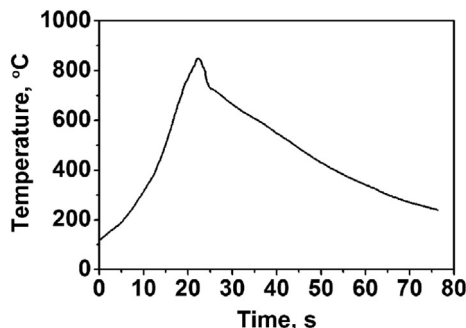


Fig. 15. Variation of transient temperature in HAZ.

When tool started moving along the welding direction, the wear band presented a lamellar distribution. The rotation rate of the tool might have an influence on the length of these bands while the welding speed affected the interval width of the bands. No Cr-depleted zone was found around the tool-wear band, thus the corrosion of this band structure in the bottom could be mainly caused by the potential difference between tool-wear particles and BM.

5. Conclusions

The pitting corrosion resistance of FSW HNS joint was investigated by immersion corrosion test and electrochemical tests. The welded joint shows relatively high corrosion resistance. The following conclusions can be drawn:

1. δ -ferrite was formed in the NZ during FSW and developed into discontinuous bands mainly in the top layer of the NZ. The continuous band observed in the bottom layer of the NZ was identified as tool wear debris. These two different band structures exhibited no obvious effect on the pitting corrosion resistance of the welded joint.
2. The protective capability of passive film of the HAZ was inferior to that of the BM during electrochemical tests, whereas the NZ showed similar protective capability to the BM. Moreover, the NZ showed a good pitting corrosion resistance during immersion test, mainly attributing to the break-up of coarse inclusions and the grain refinement during FSW.
3. No strong tendency of pitting was observed in the HAZ during immersion test, both number and size distribution densities of the

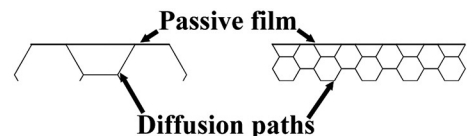


Fig. 16. Schematic of the effect of grain refining on corrosion properties.

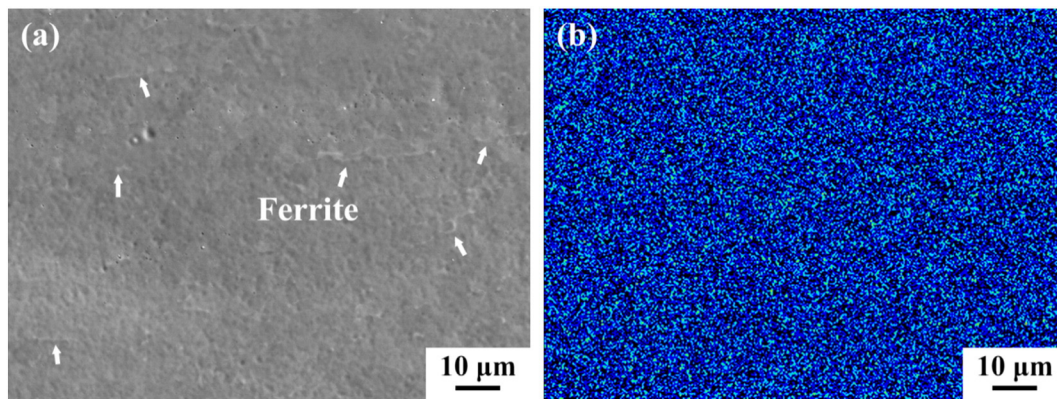


Fig. 17. Element analysis of the discontinuous bands in the top layer of NZ: (a) SEM image of the selected zone, (b) EPMA map of Cr distribution in the top layer of NZ.

HAZ were similar to those of the BM, relating to the low heat-input and high cooling rate of FSW.

Acknowledgments

This work was supported by the National Natural Science Foundation of China under grant Nos. 51201163 and 51331008.

References

- [1] E. Angelini, B. De Benedetti, F. Rosalbino, Microstructural evolution and localized corrosion resistance of an aged superduplex stainless steel, *Corros. Sci.* 46 (6) (2004) 1351–1367.
- [2] ASTM, G48-03, Standard Test Methods for Pitting and Crevice Corrosion Resistance of Stainless Steels and Related Alloys by Use of Ferric Chloride Solution, ASTM International, West Conshohocken, PA, 2003 www.astm.org.
- [3] A. Balyanov, Corrosion resistance of ultra fine-grained Ti, *Scr. Mater.* 51 (3) (2004) 225–229.
- [4] Q.X. Dai, Z.Z. Yuan, X.M. Luo, X.N. Cheng, Numerical simulation of Cr₂N age-precipitation in high nitrogen stainless steels, *Mater. Sci. Eng. A* 385 (1–2) (2004) 445–448.
- [5] B. Deng, Z. Wang, Y. Jiang, T. Sun, J. Xu, J. Li, Effect of thermal cycles on the corrosion and mechanical properties of UNS S31803 duplex stainless steel, *Corros. Sci.* 51 (12) (2009) 2969–2975.
- [6] A. Di Schino, J.M. Kenny, Grain refinement strengthening of a micro-crystalline high nitrogen austenitic stainless steel, *Mater. Lett.* 57 (12) (2003) 1830–1834.
- [7] Y. Fu, X. Wu, E.-H. Han, W. Ke, K. Yang, Z. Jiang, Effects of cold work and sensitization treatment on the corrosion resistance of high nitrogen stainless steel in chloride solutions, *Electrochim. Acta* 54 (5) (2009) 1618–1629.
- [8] S. Gao, C.S. Wu, G.K. Padhy, L. Shi, Evaluation of local strain distribution in ultrasonic enhanced Al 6061-T6 friction stir weld nugget by EBSD analysis, *Mater. Des.* 99 (2016) 135–144.
- [9] Z. Grubač, M. Metikoš-Huković, EIS study of solid-state transformations in the passivation process of bismuth in sulfide solution, *J. Electroanal. Chem.* 565 (1) (2004) 85–94.
- [10] H. Ha, H. Kwon, Effects of Cr₂N on the pitting corrosion of high nitrogen stainless steels, *Electrochim. Acta* 52 (5) (2007) 2175–2180.
- [11] U. Kamachi Mudali, P. Shankar, S. Ningshen, R.K. Dayal, H.S. Khatak, B. Raj, On the pitting corrosion resistance of nitrogen alloyed cold worked austenitic stainless steels, *Corros. Sci.* 44 (10) (2002) 2183–2198.
- [12] H. Kokawa, M. Shimada, M. Michiuchi, Z.J. Wang, Y.S. Sato, Arrest of weld-decay in 304 austenitic stainless steel by twin-induced grain boundary engineering, *Acta Mater.* 55 (16) (2007) 5401–5407.
- [13] K. Kurihara, H. Kokawa, S. Sato, Y.S. Sato, H.T. Fujii, M. Kawai, Grain boundary engineering of titanium-stabilized 321 austenitic stainless steel, *J. Mater. Sci.* 46 (12) (2011) 4270–4275.
- [14] H.B. Li, Z.H. Jiang, H. Feng, S.C. Zhang, L. Li, P.D. Han, R.D.K. Misra, J.Z. Li, Microstructure, mechanical and corrosion properties of friction stir welded high nitrogen nickel-free austenitic stainless steel, *Mater. Des.* 84 (2015) 291–299.
- [15] M. Metikoš-Huković, R. Babić, Z. Grubač, Ž. Petrović, N. Lajčić, High corrosion resistance of austenitic stainless steel alloyed with nitrogen in an acid solution, *Corros. Sci.* 53 (6) (2011) 2176–2183.
- [16] M. Michiuchi, H. Kokawa, Z.J. Wang, Y.S. Sato, K. Sakai, Twin-induced grain boundary engineering for 316 austenitic stainless steel, *Acta Mater.* 54 (19) (2006) 5179–5184.
- [17] R.S. Mishra, Z.Y. Ma, Friction stir welding and processing, *Mater. Sci. Eng. R* 50 (1–2) (2005) 1–78.
- [18] Y. Miyano, H. Fujii, Y. Sun, Y. Katada, S. Kuroda, O. Kamiya, Mechanical properties of friction stir butt welds of high nitrogen-containing austenitic stainless steel, *Mater. Sci. Eng. A* 528 (6) (2011) 2917–2921.
- [19] J. Moon, H.-Y. Ha, T.-H. Lee, Corrosion behavior in high heat input welded heat-affected zone of Ni-free high-nitrogen Fe–18Cr–10Mn–N austenitic stainless steel, *Mater. Charact.* 82 (2013) 113–119.
- [20] S.H.C. Park, Y.S. Sato, H. Kokawa, K. Okamoto, S. Hirano, M. Inagaki, Microstructure of friction-stir-welded high-nitrogen stainless steel, *Mater. Sci. Forum* 539–543 (2007) 3757–3762.
- [21] K.D. Ralston, N. Birbilis, Effect of grain size on corrosion: a review, *Corrosion* 66 (7) (2010) 075005–075005-13.
- [22] Y.S. Sato, T.W. Nelson, C.J. Sterling, R.J. Steel, C.O. Pettersson, Microstructure and mechanical properties of friction stir welded SAF 2507 super duplex stainless steel, *Mater. Sci. Eng. A* 397 (1–2) (2005) 376–384.
- [23] F. Shi, L.-j. Wang, W.-f. Cui, C.-m. Liu, Precipitation kinetics of Cr₂N in high nitrogen austenitic stainless steel, *J. Iron Steel Res. Int.* 15 (6) (2008) 72–77.
- [24] J.W. Simmons, Overview: high-nitrogen alloying of stainless steels, *Mater. Sci. Eng. A* 207 (2) (1996) 159–169.
- [25] J. Stewart, D.E. Williams, The initiation of pitting corrosion on austenitic stainless steel: on the role and importance of sulphide inclusions, *Corros. Sci.* 33 (3) (1992) 457–474.
- [26] X.Y. Wang, D.Y. Li, Mechanical and electrochemical behavior of nanocrystalline surface of 304 stainless steel, *Electrochim. Acta* 47 (24) (2002) 3939–3947.
- [27] X.Y. Wang, D.Y. Li, Mechanical, electrochemical and tribological properties of nanocrystalline surface of 304 stainless steel, *Wear* 255 (7–12) (2003) 836–845.
- [28] D. Wang, B.L. Xiao, Q.Z. Wang, Z.Y. Ma, Evolution of the microstructure and strength in the nugget zone of friction stir welded SiCp/Al–Cu–Mg composite, *J. Mater. Sci. Technol.* 30 (1) (2014) 54–60.
- [29] D. Wang, D.R. Ni, B.L. Xiao, Z.Y. Ma, W. Wang, K. Yang, Microstructural evolution and mechanical properties of friction stir welded joint of Fe–Cr–Mn–Mo–N austenitic stainless steel, *Mater. Des.* 64 (2014) 355–359.
- [30] I. Woo, Y. Kikuchi, Weldability of high nitrogen stainless steel, *ISIJ Int.* 42 (12) (2002) 1334–1343.
- [31] L.H. Wu, D. Wang, B.L. Xiao, Z.Y. Ma, Microstructural evolution of the thermomechanically affected zone in a Ti–6Al–4V friction stir welded joint, *Scr. Mater.* 78–79 (2014) 17–20.
- [32] R.Z. Xu, D.R. Ni, Q. Yang, C.Z. Liu, Z.Y. Ma, Pinless friction stir spot welding of Mg–3Al–1Zn alloy with Zn interlayer, *J. Mater. Sci. Technol.* 32 (1) (2016) 76–88.
- [33] P. Xue, Y. Komizo, R. Ueji, H. Fujii, Enhanced mechanical properties in friction stir welded low alloy steel joints via structure refining, *Mater. Sci. Eng. A* 606 (2014) 322–329.
- [34] S. Yoon, R. Ueji, H. Fujii, Effect of initial microstructure on Ti–6Al–4V joint by friction stir welding, *Mater. Des.* 88 (2015) 1269–1276.
- [35] S.J. Zheng, Y.J. Wang, B. Zhang, Y.L. Zhu, C. Liu, P. Hu, X.L. Ma, Identification of MnCr₂O₄ nano-octahedron in catalysing pitting corrosion of austenitic stainless steels, *Acta Mater.* 58 (15) (2010) 5070–5085.